The Deep SPIRE HerMES Survey: spectral energy distributions and their astrophysical indications at high redshift

D. Brisbin, M. Harwit, B. Altieri, A. Amblard, V. Arumugam, H. Aussel, T. Babbedge, A. Blain, J. Bock, A. Boselli, et al.

Monthly Notices
of the
ROYAL ASTRONOMICAL SOCIETY

Mon. Not. R. Astron. Soc. **409,** 66–74 (2010) doi:10.1111/j.1365-2966.2010.17643.x

The Deep SPIRE HerMES Survey: spectral energy distributions and their astrophysical indications at high redshift

D. Brisbin,[1⋆] M. Harwit,[2] B. Altieri,[3] A. Amblard,[4] V. Arumugam,[5] H. Aussel,[6] T. Babbedge,[7] A. Blain,[8] J. Bock,[8,9] A. Boselli,[10] V. Buat,[10] N. Castro-Rodríguez,[11,12] A. Cava,[11,12] P. Chanial,[6] D. L. Clements,[7] A. Conley,[13] L. Conversi,[3] A. Cooray,[4,8] C. D. Dowell,[8,9] E. Dwek,[14] S. Eales,[15] D. Elbaz,[6] M. Fox,[7] A. Franceschini,[16] W. Gear,[15] J. Glenn,[13] M. Griffin,[15] M. Halpern,[17] E. Hatziminaoglou,[18] E. Ibar,[19] K. Isaak,[15] R. J. Ivison,[5,19] G. Lagache,[20] L. Levenson,[8,9] Carol J. Lonsdale,[21] N. Lu,[8,22] S. Madden,[6] B. Maffei,[23] G. Mainetti,[16] L. Marchetti,[16] G. E. Morrison,[24,25] H. T. Nguyen,[8,9] B. O'Halloran,[7] S. J. Oliver,[26] A. Omont,[27] F. N. Owen,[21] M. Pannella,[21] P. Panuzzo,[6] A. Papageorgiou,[15] C. P. Pearson,[28,29] I. Pérez-Fournon,[11,12] M. Pohlen,[15] D. Rizzo,[7] I. G. Roseboom,[26] M. Rowan-Robinson,[7] M. Sánchez Portal,[3] B. Schulz,[8,22] N. Seymour,[30] D. L. Shupe,[8,22] A. J. Smith,[26] J. A. Stevens,[31] V. Strazzullo,[21] M. Symeonidis,[30] M. Trichas,[32] K. E. Tugwell,[30] M. Vaccari,[16] I. Valtchanov,[3] L. Vigroux,[27] L. Wang,[26] R. Ward,[26] G. Wright,[19] C. K. Xu[8,22] and M. Zemcov[8,9]

[1]*Space Science Building, Cornell University, Ithaca, NY 14853-6801, USA*
[2]*Cornell University and 511 H Street, SW, Washington, DC 20024-2725, USA*
[3]*Herschel Science Centre, European Space Astronomy Centre, Villanueva de la Cañada, 28691 Madrid, Spain*
[4]*Department of Physics & Astronomy, University of California, Irvine, CA 92697, USA*
[5]*Institute for Astronomy, University of Edinburgh, Royal Observatory, Blackford Hill, Edinburgh EH9 3HJ*
[6]*Laboratoire AIM-Paris-Saclay, CEA/DSM/Irfu – CNRS – Université Paris Diderot, CE-Saclay, pt courrier 131, F-91191 Gif-sur-Yvette, France*
[7]*Astrophysics Group, Imperial College London, Blackett Laboratory, Prince Consort Road, London SW7 2AZ*
[8]*California Institute of Technology, 1200 E. California Blvd, Pasadena, CA 91125, USA*
[9]*Jet Propulsion Laboratory, 4800 Oak Grove Drive, Pasadena, CA 91109, USA*
[10]*Laboratoire d'Astrophysique de Marseille, OAMP, Université Aix-marseille, CNRS, 38 rue Frédéric Joliot-Curie, 13388 Marseille cedex 13, France*
[11]*Instituto de Astrofísica de Canarias (IAC), E-38200 La Laguna, Tenerife, Spain*
[12]*Departamento de Astrofísica, Universidad de La Laguna (ULL), E-38205 La Laguna, Tenerife, Spain*
[13]*Department of Astrophysical and Planetary Sciences, CASA 389-UCB, University of Colorado, Boulder, CO 80309, USA*
[14]*Observational Cosmology Lab, Code 665, NASA Goddard Space Flight Center, Greenbelt, MD 20771, USA*
[15]*Cardiff School of Physics and Astronomy, Cardiff University, Queens Buildings, The Parade, Cardiff CF24 3AA*
[16]*Dipartimento di Astronomia, Università di Padova, vicolo Osservatorio, 3, 35122 Padova, Italy*
[17]*Department of Physics & Astronomy, University of British Columbia, 6224 Agricultural Road, Vancouver, BC V6T 1Z1, Canada*
[18]*ESO, Karl-Schwarzschild-Str. 2, 85748 Garching bei München, Germany*
[19]*UK Astronomy Technology Centre, Royal Observatory, Blackford Hill, Edinburgh EH9 3HJ*
[20]*Institut d'Astrophysique Spatiale (IAS), bâtiment 121, Université Paris-Sud 11 and CNRS (UMR 8617), 91405 Orsay, France*
[21]*National Radio Astronomy Observatory, PO Box O, Socorro, NM 87801, USA*
[22]*Infrared Processing and Analysis Center, MS 100-22, California Institute of Technology, JPL, Pasadena, CA 91125, USA*
[23]*School of Physics and Astronomy, The University of Manchester, Alan Turing Building, Oxford Road, Manchester M13 9PL*
[24]*Institute for Astronomy, University of Hawaii, Honolulu, HI 96822, USA*
[25]*Canada–France–Hawaii Telescope, Kamuela, HI 96743, USA*
[26]*Astronomy Centre, Department of Physics & Astronomy, University of Sussex, Brighton BN1 9QH*
[27]*Institut d'Astrophysique de Paris, UMR 7095, CNRS, UPMC Univ. Paris 06, 98bis boulevard Arago, F-75014 Paris, France*
[28]*Space Science & Technology Department, Rutherford Appleton Laboratory, Chilton, Didcot, Oxfordshire OX11 0QX*
[29]*Institute for Space Imaging Science, University of Lethbridge, Lethbridge, Alberta T1K 3M4, Canada*
[30]*Mullard Space Science Laboratory, University College London, Holmbury St Mary, Dorking, Surrey RH5 6NT*

⋆E-mail: brisbind@astro.cornell.edu

[31] *Centre for Astrophysics Research, University of Hertfordshire, College Lane, Hatfield, Hertfordshire AL10 9AB*
[32] *Harvard–Smithsonian Center for Astrophysics, 60 Garden Street, Cambridge, MA 02138, USA*

Accepted 2010 September 3. Received 2010 September 2; in original form 2010 June 11

ABSTRACT

The Spectral and Photometric Imaging Receiver on-board *Herschel* has been carrying out deep extragalactic surveys, one of the aims of which is to establish spectral energy distributions of individual galaxies spanning the infrared/submillimetre (IR/SMM) wavelength region. We report observations of the IR/SMM emission from the Lockman North field and Great Observatories Origins Deep Survey Field-North. Because galaxy images in the wavelength range covered by *Herschel* generally represent a blend with contributions from neighbouring galaxies, we present sets of galaxies in each field, especially free of blending at 250, 350 and 500 μm. We identify the cumulative emission of these galaxies and the fraction of the FIR cosmic background radiation they contribute. Our surveys reveal a number of highly luminous galaxies at redshift $z \lesssim 3$ and a novel relationship between IR and visible emission that shows a dependence on luminosity and redshift.

Key words: galaxies: high-redshift – galaxies: starburst – galaxies: star formation – infrared: galaxies.

1 INTRODUCTION

The *Herschel*[1] *Space Observatory* (Pilbratt et al. 2010) has opened wide astronomical access to the far-infrared/submillimetre (FIR/SMM) spectral range. With the Spectral and Photometric Imaging Receiver (SPIRE) (Griffin et al. 2010), deep cosmological surveys are studying galaxies out to redshifts of the order of $z \sim 3$, reaching back to epochs when the Universe was only a few billion years old.

A primary motivation for these surveys, as well as those undertaken with the Photodetector Array Camera & Spectrometer (PACS) on-board *Herschel* (Poglitsch et al. 2010), is to gain improved spectral energy distributions (SEDs) of astronomical sources. With an appropriate redshift, integration of the flux densities demarcated by the SEDs permits derivation of rest-frame luminosities, star formation rates (SFRs) and other physical properties of galaxies.

Among the first observations undertaken by the SPIRE in the Herschel Multi-tiered Extragalactic Survey (HerMES[2]) project (Oliver et al. 2010) have been surveys of galaxies in the Great Observatories Origins Deep Survey Field-North (GOODS-N) and northern portions of the Lockman Hole (Lockman North, hereinafter LN) field [see Oliver et al. (2010) for a description of these early observations]. Source confusion, as defined and discussed in detail by Takeuchi & Ishii (2004), results in blending of FIR sources and complicates the analysis of survey data. In light of the large degree of source blending expected at SPIRE wavelengths, novel options for source extraction have been pursued (Béthermin et al. 2010; Roseboom et al. 2010; Smith et al. in preparation). Rather than looking for sources based on SPIRE intensity maps alone or relying on traditional source detection and extraction techniques for the SPIRE data, which are heavily affected by confusion, Roseboom et al. (2010) measure the SPIRE flux at the position of known 24-μm sources using a linear inversion technique to account for source blending. The rationale for this is provided by the results of the Balloon-borne Large Aperture Submillimetre Telescope (BLAST) extragalactic survey (Marsden et al. 2009), which showed that the 24-μm and the FIR flux densities are at least statistically correlated.

[1] *Herschel* is an ESA space observatory with science instruments provided by the European-led Principal Investigator consortia and with important participation from the NASA.
[2] hermes.sussex.ac.uk

2 PRIMARY AIMS

The aims of this paper are two-fold; our primary aim is to derive SEDs for distant galaxies observed by the SPIRE. Before this can be achieved, however, a robust way of identifying sources least affected by confusion and blending must be devised.

The GOODS-N catalogue of Roseboom et al. (2010) provides a cross-identification (XID) of the FIR/SMM flux density at 250, 350 and 500 μm with 1951 possible 24-μm counterparts having minimum flux densities of 20 μJy. Many of the identified 24-μm galaxies are further cross-identified with ultraviolet, optical, near-IR and radio counterparts. The survey covered a 12.3×18.6 arcmin strip, corresponding to $\sim$230 arcmin^2.

The SPIRE beam diameters at full width at half-maximum (FWHM), respectively, measure 18.1, 25.2 and 36.9 arcsec at 250, 350 and 500 μm. For present purposes, we take the beams to be close to circular; their ellipticity varies from pixel to pixel, but is approximately 1.08 ± 0.05, the longer direction lying in the spacecraft horizontal direction, parallel to the ecliptic plane (Bernhard Schulz, private communication). The beam at 500 μm thus has an area $\sim$0.3 arcmin^2. With 1951 possible 24-μm sources, we can expect a typical 500-μm beam to contain 2.5 possible sources. At 250 μm, the crowding is a factor of 4 less severe, but still appreciable. An example of the crowded source distribution is seen in Fig. 1 where the SPIRE beam outlines are overlaid on a patch of the GOODS-N field centred on a 24-μm source.

In the Northern Lockman region, a 40.1×36.2 arcmin^2 segment of the sky yielded 6316 possible 24-μm counterparts with minimum flux densities of 50 μJy in an area subtending $\sim$1500 arcmin^2 – again

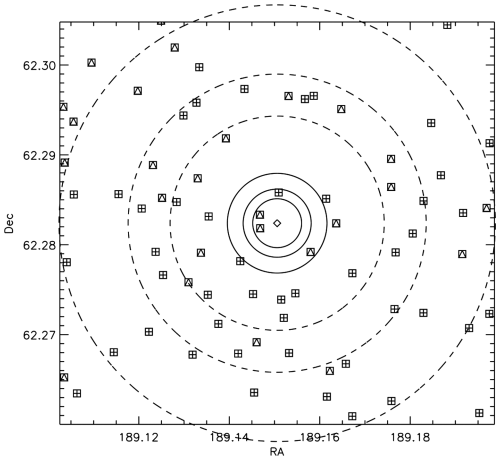

Figure 1. A GOODS-N SPIRE and 24-μm source with equatorial coordinates (J2000.0) 189.1506/62.2824 shown as a diamond with nearby 24-μm sources. Known ambient 24-μm sources are shown as squares with nested symbols. Plus signs indicate sources with known redshifts and triangles indicate sources with unknown redshift. The spatial distribution of 24-μm sources is based on the XID information in Roseboom et al. (2010). The solid circles represent the FWHM of the Airy profile PRF at the three SPIRE wavelengths and dashed circles represent the second Airy minimum. Coordinates are in J2000.

corresponding to more than one potential 500-μm source per beam. Identification of sources least affected by confusion and blending is therefore important. These sources have also been cross-identified at multiple wavelengths and assigned photometric redshifts as detailed in Strazzullo et al. (2010).

3 DATA

Using the existing high spatial resolution *Spitzer* 24-μm data and the known FIR instrumental point response function (PRF) as inputs, Roseboom et al. (2010) determined best-fitting 250, 350, and 500-μm fluxes by a procedure they detailed in their paper. In each SPIRE wavelength band, their tabulated XIDs provide both their best estimate of the flux density, F_ν, and the flux density PRF_ν in a PRF-convolved map centred on the position of an associated 24-μm source. They make no assumptions about a proportionality between 24-μm and FIR flux densities, but assume that SPIRE sources will only be detected at positions of 24-μm sources. For each source, ancillary data at other wavelengths are included, as well as several flags that can be used to identify degenerate cases. Of particular importance is the redshift of the associated 24-μm source, which enables derivation of rest-frame SEDs and thus source luminosities. Wherever we refer to F_ν and PRF_ν in the remainder of this paper, these quantities are to be thought of as those defined by Roseboom et al. (2010).

The flux density in a PRF-convolved region centred on the position of the 24-μm galaxy associated with each FIR source represents the system response not only to the flux density attributed to this source (referred to as $F_\nu|_\lambda$), but also to contributions from nearby sources. It thus provides a measure of blending, characterizing each source. We define a *purity index* Π_λ for each source as the ratio

$$\Pi_\lambda = F_\nu/\mathrm{PRF}_\nu|_\lambda \quad (1)$$

where λ specifies the wavelength band, 250, 350 or 500 μm, and $\mathrm{PRF}_\nu|_\lambda$, as supplied in the XID catalogues by Roseboom et al. (2010), is the PRF-smoothed flux density at the position of the source.[3] A high value of Π_λ indicates low confusion and blending in wavelength band λ; a low value indicates high blending. The fractional contributions by ambient sources to the PRF-convolved flux density within a PRF is simply $(1 - \Pi_\lambda)$. In principle, the purity index must assume values $0 \lesssim \Pi_\lambda \lesssim 1$. In practice, however, the value F_ν has been calculated *on top of* a locally determined background, whereas the PRF_ν values do not take a local background variation into account. This can result in $\Pi_\lambda > 1$ when a negative local background or 'baseline' has been used.

4 THE STATISTICS OF PURITY INDICES IN THE GOODS-N AND LOCKMAN NORTH

We have found it useful to identify sources whose purity indices exceed Π_λ measures of 0.7, 0.5 and 0.3 at 250, 350 and 500 μm, respectively. We say that a source is *secure* at each wavelength if it meets this criterion. If the source is found to be secure in all three wavelength bands, we call it *triply secure*. High-purity sources are of special interest, because their isolated nature makes them less susceptible to blending by neighbours. It is these sources, which will be especially useful for follow-up studies with other instruments and may also provide confirmation of the deblending approach used. It should be noted, however, that a flux density estimate from a highly pure source might still be inaccurate, if there is significant contribution from an IR source that is not observed at 24 μm. Furthermore, sources with low purity do have well-defined deblending solutions and hence well-characterized flux densities and uncertainties from Roseboom et al. (2010). In crowded fields, the true flux density is very likely described by this characterization, although the margins of uncertainty tend to be large. Our choice of purity criteria is somewhat subjective, but offers a reasonable compromise for extracting relatively reliable SEDs despite source blending. Understandably, these criteria may be expected to vary depending on the type of information an astronomer expects to extract from the survey data.

When a reliable redshift is available, the single most important quantity that can be determined from an SED is source luminosity. With this, one can begin discussing the luminosity distribution at specific redshifts, as well as luminosity evolution as a function of redshift, particularly among ultraluminous galaxies that emit the dominant fraction of their energy in the IR. However, to obtain a reliable SED and thus a reliable luminosity, we require sources whose flux densities are well determined at all three SPIRE wavelengths in order to optimally constrain the flux density defining the broad wavelength region around peak emission.

To explain the consequences of our choice of purity criteria in this context, we may consider a toy model which, as pointed out in Section 1, will exhibit an average number of sources $n_\lambda \sim 2.5$, 1.225 and 0.625 per GOODS-N beam at 500, 350 and 250 μm, respectively. Let us inject an additional source into such a beam and call it the primary source. If all the sources involved are equally bright, on average, that is, make equal contributions to the PRF-smoothed flux density, the purity of the primary source will be $\Pi_\lambda = (1 + n_\lambda)^{-1}$, that is, 0.29, 0.45 and 0.62 at 500, 350 and 250 μm, respectively. Half of the sources in each waveband will have purities higher than these purity cuts, and half lower.

[3] Our $\mathrm{PRF}_\nu|_\lambda$ corresponds to the quantity **d** in equation (2) of Roseboom et al. (2010), convolved with the PRF centred on the primary source whose flux is $F_\nu|_\lambda$. The entries in the XID tables list our $F_\nu|_\lambda$ as $F(\lambda)$ and our $\mathrm{PRF}_\nu|_\lambda$ flux density as PRF(λ).

Table 1. Fraction of detected SPIRE sources in the GOODS-N and LN with a Π_λ value greater than the threshold indicated in the top row. For the GOODS-N and LN regions we place an upper limit cut-off on Π_λ of 1.1 and 1.2 respectively. The columns marked 'detections' denote the total number of SPIRE sources detected at a given wavelength in the present HerMES project.

			GOODS-N		
$\Pi >$	0.9	0.7	0.5	0.3	Detections
250 μm	0.106	0.231	0.348	0.493	1032
350 μm	0.069	0.199	0.316	0.451	697
500 μm	0.061	0.141	0.227	0.362	475
			LN		
$\Pi >$	0.9	0.7	0.5	0.3	Detections
250 μm	0.275	0.435	0.579	0.703	4646
350 μm	0.184	0.343	0.500	0.670	2968
500 μm	0.144	0.281	0.419	0.570	2127

Turning now to our preferred adoption of purity cuts of 0.3, 0.5 and 0.7 at 500, 350 and 250 μm, respectively, we see that they assure two properties: (i) that they yield sources whose purities are above average at all three wavelengths, and (ii) that the fraction of sources with purity above the cut is roughly comparable at all three wavelengths – a balance, which is important to assure a well-defined SED. Table 1, described below, confirms these traits for the GOODS-N sample. It shows that a fraction $f_\lambda = 0.23$ of the sources has purity exceeding 0.7 at 250 μm, a fraction 0.32 exceeding purity 0.5 at 350 μm and a fraction 0.36 exceeding purity 0.3 at 500 μm. These fractions cluster around a value of 0.3, thus lending roughly equal weight to the flux density in each waveband in the determination of the SED.

In Table 1, we list the fraction of sources in the GOODS-N and LN whose purity indices lie above certain cuts. We permit these indices to slightly exceed a value of 1, with a cut-off of $\Pi = 1.1$ in the GOODS-N and $\Pi = 1.2$ in the LN. These relaxed upper limits are designed to allow the inclusion of detections with a significant local background, which otherwise have all the earmarks of being secure.

In the GOODS-N region, the XID catalogue lists 183 sources observed at all three wavelengths and with known redshift, 16 of which are triply secure. If we remove the upper limit $\Pi = 1.1$, the number of triply secure sources rises to 59. In the LN, there are 633 sources with detections at all five wavelengths with known redshift, 165 of which are triply secure; this number increases to 287, if we remove the upper limits on purity. Although the numbers of these galaxies are quite modest, they nevertheless yield informative statistics on the luminosities and luminosity distributions of galaxies observed out to redshifts $z \sim 3$. These will be discussed in Section 6.

The larger aperture of the *Herschel* telescope and the higher spatial resolution have permitted the SPIRE surveys to reach depths beyond those attained by the BLAST. Nevertheless, Marsden et al. (2009) succeeded in acquiring reliable measurements of stacked source flux densities at comparable wavelengths. Their results indicate surface brightnesses of 8.60 ± 0.59, 4.93 ± 0.34 and 2.27 ± 0.20 nW m^{-2} sr^{-1} at 250, 350 and 500 μm, respectively. These stacked source flux densities represent the major component of the cosmic infrared background (CIB) measured by the Cosmic Background Explorer's Far-Infrared Absolute Spectrometer (FIRAS) to be 10.4 ± 2.3, 5.4 ± 1.6 and 2.4 ± 0.6 nW m^{-2} sr^{-1} at 250, 350 and 500 μm, respectively (Fixsen et al. 1998). To investigate the extent to which this background is resolved with *Herschel*, we summed the estimated flux densities for our secure SPIRE sources in the deepest field (GOODS-N) and then attributed this flux density to the entire survey region of 230 arcmin^2. Using the flux densities for sources contained in the XID catalogue of Roseboom et al. (2010), our cumulative surface brightness for the GOODS-N at 250, 350 and 500 μm is 1.49, 0.70 and 0.41 nW m^{-2} sr^{-1} or 14, 13 and 17 per cent of the estimated CIB, respectively. At 250 and 350 μm, these values are within 1σ of those corrected for blending and incompleteness by Oliver et al. (2010).

5 SPECTRAL ENERGY DISTRIBUTION OF THE SECURE SOURCES

Figs 2 and 3 exhibit SEDs for triply secure sources in the LN and GOODS-N. For LN sources, we have set an additional criterion for inclusion, namely that they have observed flux densities also at PACS wavelengths of 100 and 170 μm. Along with examining the observed SED, we show a fit using starburst models developed by Siebenmorgen & Krügel (2007) (hereinafter S&K). These models are based on a nuclear concentration of massive young stars embedded in a matrix of gas and dust referred to as 'hotspots'. S&K use a five-parameter SED fit, which incorporates a variable nuclear bulge size with old and new stellar components as well as the effects of dust. They provide their models in the form of a library of 7000 SEDs available as text files online.[4] By using their models, we are able to not only find realistic intrinsic luminosities, but also SFRs for highly luminous sources at high redshift for which the Kennicut IR–SFR relations apply (Kennicutt 1998).

The S&K model fits observations quite well, although some of our SEDs exhibit considerable deviations from the data at visible and near-IR wavelengths. This is largely due to variable shielding of starlight by dust (see Section 6 below).

In Figs 2 and 3, we have focused on high-redshift ($z > 0.5$) sources as these are of greatest interest to star formation history. Tables 2 and 3 show the luminosities and SFRs of galaxies whose SEDs are shown in Figs 2 and 3. The models appear capable of correctly representing the galaxies we observe, most of which are highly luminous and likely to be starbursts. Like most present models, however, vastly different dust masses and nuclear sizes are able to yield similar SEDs, as witnessed by the large differences in dust masses assigned to some galaxies listed in Tables 2 and 3 that have nearly identical redshifts and luminosities. This is not surprising because the models are only required to provide sufficient dust to convert most of the visible and ultraviolet radiation produced in the starburst into IR radiation at the observed temperature. If this criterion is satisfied, the models produce roughly correct SEDs.

While these figures and tables emphasize the relatively few triply-secure SEDs among high-redshift objects, it is important to note that for many statistical trends, triple-security is not necessary. In Fig. 4, we show the luminosities we have determined as a function of redshift, based on the S&K models for all sources in the GOODS-N and LN that have detections of any kind (secure or not) at all three SPIRE bands. While some of the flux densities, especially at 500 μm, are quite uncertain (see Figs 2 and 3), this will not greatly affect the overall luminosity distribution. We estimate the source luminosity uncertainty to be ∼20 per cent. The minimum

[4] The S&K SED library of models is available at http://www.eso.org/∼rsiebenm/sb_models/.

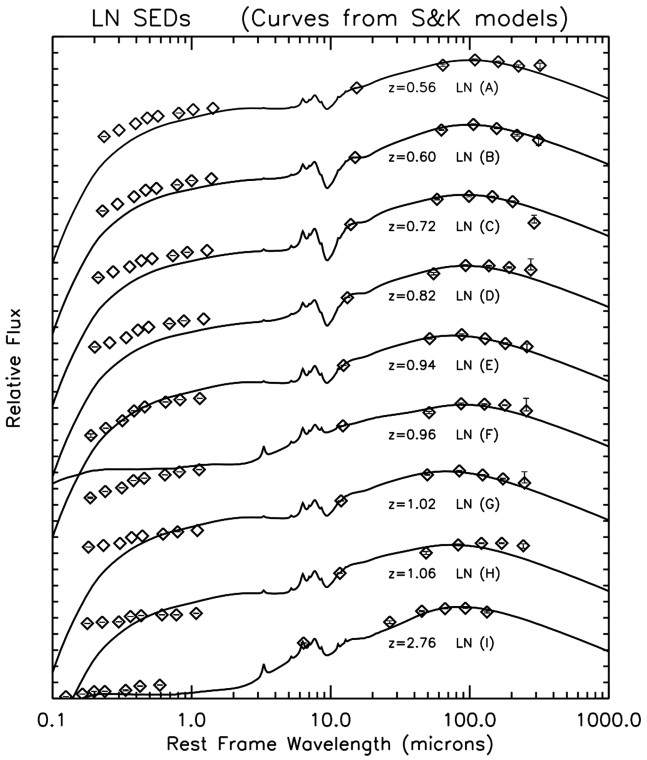

Figure 2. LN galaxy SEDs plotted with arbitrary flux density offsets. These galaxies all met or exceeded our selection criteria of being securely identified at all three wavelengths, having a high purity index (30, 50 and 70 per cent pure at 500, 350 and 250 μm, respectively), having known PACS detections at 100 and 170 μm and redshifts $z > 0.5$. Each tick mark on the y-axis indicates a change by a factor of 10. Observed flux densities are indicated by diamonds. For most observations, the error bars are smaller than the diamond; however, for LN sources C, D, F and G, the 500-μm measurement is compatible with zero, so we have plotted only the upper error bar. The solid line is an S&K model fit to the 24–500 μm error-weighted observations. We weighted the 24-μm observations only a quarter as heavily as the longer wavelengths, which play a dominant role in determining starburst luminosities. Observational data shortwards of 24 μm are plotted for reference, but not used in fitting. Source values of Π are shown in Table 2. As with many of the examples quoted by S&K, the visual component of the SED often needs to be fitted by hand, because it bears a little relation to the starburst characteristics responsible for the mid- and far-IR flux densities. The extent to which visible stars may or may not contribute to the SED is determined in part by the degree to which an older population of stars is obscured by dust without significantly contributing to its heating or by massive young stars whose shrouding by dust has gradually declined. Shrouding by dust may explain the significant drop in optical luminosities exhibited by some of the sources at the shortest wavelengths.

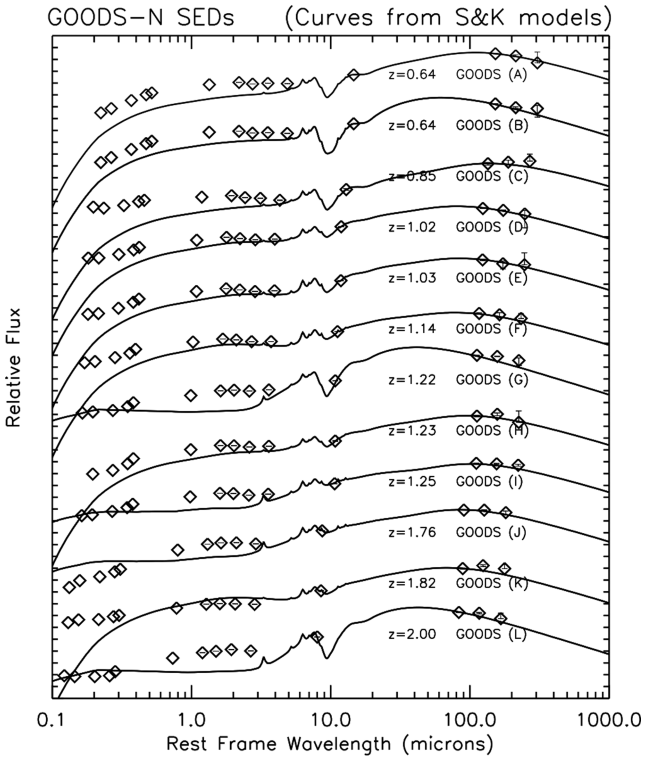

Figure 3. GOODS-N galaxy SEDs plotted as in Fig. 2. The 500-μm measurements for the GOODS-N sources A, C, E, F, H, K and L are compatible with zero, so here we plot only the upper error bar, barely visible within the diamond symbol. As in Fig. 2, we weighted the 24-μm data a quarter as heavily as the longer wavelengths. Observational data shortwards of 24 μm are plotted for reference but not used in fitting.

detectable luminosities follow the expected trend of increasing with the square of luminosity distance (which we determined based on a $\Lambda = 0.7$, $H_0 = 70$ km s^{-1} Mpc^{-1} cosmology).

Throughout this paper, we refer to multiple luminosities, namely total bolometric luminosity and IR luminosity integrated over 8–1000 μm [as used in star formation estimates by Kennicutt (1998)]. For our purposes, the difference between the two is small as the majority of a luminous star-forming galaxy's energy is emitted in the IR. In galaxies with $L_{\rm IR} \gtrsim 10^{11.5}\,{\rm L}_{\odot}$, Buat et al. (2010) find that ∼95 per cent of the total SFR is accounted for by $L_{\rm IR}$. None the less, we explicitly differentiate between the two when the distinction is significant.

6 THE NATURE OF THE ULTRALUMINOUS SOURCES

As Fig. 4 attests, our surveys reveal a number of highly luminous sources, mainly at redshifts between $z = 2.5$ and 3.2. Discussing all of these in detail is beyond the scope of this paper, if for no other reason than that information on these sources is still quite modest. Nevertheless, we here discuss four of these sources to show that their luminosities appear to be intrinsic. Neither gravitational lensing nor blending from neighbouring sources appears to contribute significantly to the observed luminosities. This may not be true of all of the luminous SPIRE sources, but it appears to be so for at least those about which we have the most information right now. A number of other uncertainties also warrant comment.

(i) For most of the sources observed in LN, only photometric redshifts are available. For the more luminous sources shown, estimated redshift errors range from ∼6 to 17 per cent in the catalogues of Roseboom et al. (2010). Because calculated luminosities are proportional to $(1 + z)^2$, a 17 per cent error at $z = 2.5$ can lead to a luminosity error in the range of ∼23–26 per cent. For sources with established spectroscopic redshifts, the uncertainty is far smaller and can be neglected.

(ii) A second area of concern is discrimination between intrinsically luminous sources and sources that may be lensed by foreground galaxies to merely appear luminous. For some purposes, for example, accounting for sources contributing to the diffuse background, this distinction may not be of primary importance; but for

Table 2. Data on LN galaxies whose SEDs appear in Fig. 2. We list the ID as established by Roseboom et al. (2010), right ascension (RA) and declination (Dec.) (J2000), photometric redshift $z > 0.5$, our purity indices Π_λ, total bolometric luminosity as estimated by an S&K model, SFR based on the IR–luminosity relation (Kennicutt 1998) and dust mass estimated by the S&K model. Along with these derived parameters, we list the model parameters: nuclear radius, visual extinction to centre (A_V) and gas density within hotspots ($n_{\rm hs}$).

ID	RA	Dec.	z	$L_{\rm bolometric}$ ($L_\odot$)	SFR ($M_\odot\,{\rm yr}^{-1}$)	$M_{\rm dust}$ ($M_\odot$)	Π_{250}	Π_{350}	Π_{500}	Radius (kpc)	A_V	$\log_{10}(n_{\rm hs} \times {\rm cm}^3)$
LN (A)	161.8365	59.1211	0.56	4.0×10^{11}	66	1.6×10^8	0.89	0.67	0.74	3.0	35.9	3
LN (B)	161.5001	58.8732	0.60	7.9×10^{11}	130	3.2×10^8	0.74	0.62	0.88	3.0	72.0	4
LN (C)	161.1277	59.1956	0.72	1.3×10^{12}	210	3.2×10^8	1.10	1.00	1.07	3.0	72.0	2
LN (D)	161.3232	59.2086	0.82	1.3×10^{12}	210	3.2×10^8	0.88	0.80	0.98	3.0	72.0	4
LN (E)	161.0530	59.0762	0.94	2.0×10^{12}	330	1.6×10^8	0.92	0.65	0.69	3.0	35.9	3
LN (F)	161.3680	59.2242	0.96	2.5×10^{12}	400	3.6×10^8	0.96	0.97	0.56	9.0	9.0	4
LN (G)	161.3429	59.2269	1.02	4.0×10^{12}	650	1.6×10^8	0.89	0.87	0.64	3.0	35.9	2
LN (H)	161.4871	58.8886	1.06	2.5×10^{12}	410	1.6×10^8	0.76	0.82	0.93	3.0	35.9	2
LN (I)	161.8669	58.8708	2.76	2.5×10^{13}	4300	4.9×10^9	0.91	0.96	0.77	9.0	120.0	4

Table 3. Data on GOODS-N galaxies whose SEDs appear in Fig. 3, listed as in Table 2. The redshifts here are spectroscopic.

ID	RA	Dec.	z	$L_{\rm bolometric}$ ($L_\odot$)	SFR ($M_\odot\,{\rm yr}^{-1}$)	$M_{\rm dust}$ ($M_\odot$)	Π_{250}	Π_{350}	Π_{500}	Radius (kpc)	A_v	$\log_{10}(n_{\rm hs} \times {\rm cm}^3)$
GOODS (A)	189.0274	62.1643	0.6380	5.0×10^{11}	84	3.2×10^8	0.83	0.84	0.44	3.0	72.0	4
GOODS (B)	189.3938	62.2898	0.6402	2.0×10^{12}	340	6.0×10^7	0.98	0.64	0.90	1.0	119.0	2
GOODS (C)	189.2979	62.1820	0.8549	1.3×10^{11}	21	3.2×10^8	1.00	0.81	0.74	3.0	72.0	4
GOODS (D)	189.1403	62.1683	1.0160	1.6×10^{12}	260	1.6×10^8	0.99	0.75	0.54	3.0	35.9	3
GOODS (E)	189.0633	62.1691	1.0270	1.3×10^{12}	210	1.6×10^8	0.92	0.52	0.45	3.0	35.9	2
GOODS (F)	189.3171	62.3541	1.1440	1.0×10^{12}	160	8.1×10^7	0.73	0.68	0.68	3.0	17.9	2
GOODS (G)	189.1438	62.2114	1.2242	2.5×10^{13}	4300	6.0×10^7	0.88	0.89	0.98	1.0	119.0	4
GOODS (H)	189.2137	62.1810	1.2258	6.3×10^{11}	100	1.6×10^8	0.71	0.83	0.31	3.0	35.9	4
GOODS (I)	189.2614	62.2338	1.2480	1.3×10^{12}	200	3.6×10^8	0.98	0.93	0.97	9.0	9.0	4
GOODS (J)	189.2566	62.1962	1.7600	6.3×10^{12}	1000	7.3×10^8	1.02	1.04	1.03	9.0	18.0	4
GOODS (K)	189.3036	62.1955	1.8150	2.0×10^{12}	310	8.1×10^7	1.08	0.86	0.50	3.0	17.9	3.4
GOODS (L)	189.0764	62.2640	2.0000	2.0×10^{13}	3400	6.0×10^7	0.82	0.71	0.33	1.0	119.0	2

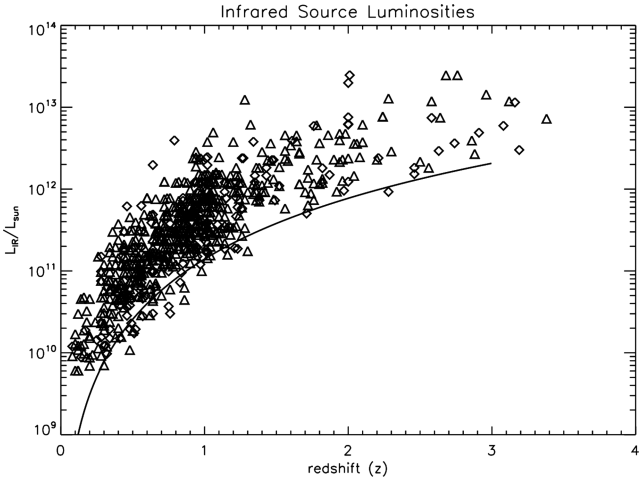

Figure 4. IR source luminosities (integrated over 8–1000 μm) in the GOODS-N and LN plotted as a function of redshift for all sources detected at all three SPIRE wavelengths. Diamonds indicate GOODS-N luminosities obtained from SEDs fitted by S&K models and triangles indicate similar luminosities for LN sources. The solid line shows the growth of luminosity distance squared with z. It serves as a rough lower bound to the luminosities in our selection of observed sources; the scatter of data points about the curve provides a visual impression of the uncertainties in those luminosities.

charting the luminosities of distant sources, their intrinsic luminosities need to be determined.

(iii) Because our deep surveys are highly sensitive, they reveal a large number of faint sources. This leads to potential misidentification of sources. It can also lead to blending. However, seven of the 11 ultraluminous sources in Fig. 5 and Table 4 are triply secure; the remaining four are doubly secure within observational uncertainties. Severe blending is thus unlikely.

(iv) For some of the sources, the available data points straddle but do not directly constrain the region where the SED reaches a maximum (see Fig. 5), so that our SED-derived luminosities could be overestimated.

At the present stage of data reduction, we are not yet in a position to account for all these uncertainties. However, for the cited sources in the GOODS-N and for a few sources in LN, reliable spectroscopic redshifts are available. In four of these, we were able, below, to search for potential lensing, assess a degree of blending and justify our confidence in their derived luminosities in some detail. These sources are referred to by letters corresponding to their designations in Table 4. Note that in Table 4 we give bolometric luminosities, whereas below we quote IR luminosities.

The LN source (j) at equatorial position (J2000.0) 161.554052/58.788592 is characterized in the Sloan Digital Sky Survey as a well-isolated circular source identified as a quasi-stellar object (QSO). The visible spectrum leaves no doubt about the redshift $z = 3.037$ determined by the strong Lyα line. The visible continuum flux in this spectrum is $\sim 5 \times 10^{-17}$ erg cm^{-2} s^{-1} Å^{-1}, equivalent to $\sim 4 \times 10^{-5}$ Jy, stretching down to $\sim$1000 Å, for a total flux of roughly 1.2×10^{-15} W m^{-2}, which is comparable to the IR flux observed from the source. The IPAC extragalactic data base lists the optical source as brighter, by more than a magnitude, than any other source within a radius of 1 arcmin. Trouille et al. (2008) list a 0.5–2 keV X-ray flux of 38.4×10^{-18} W m^{-2} and a

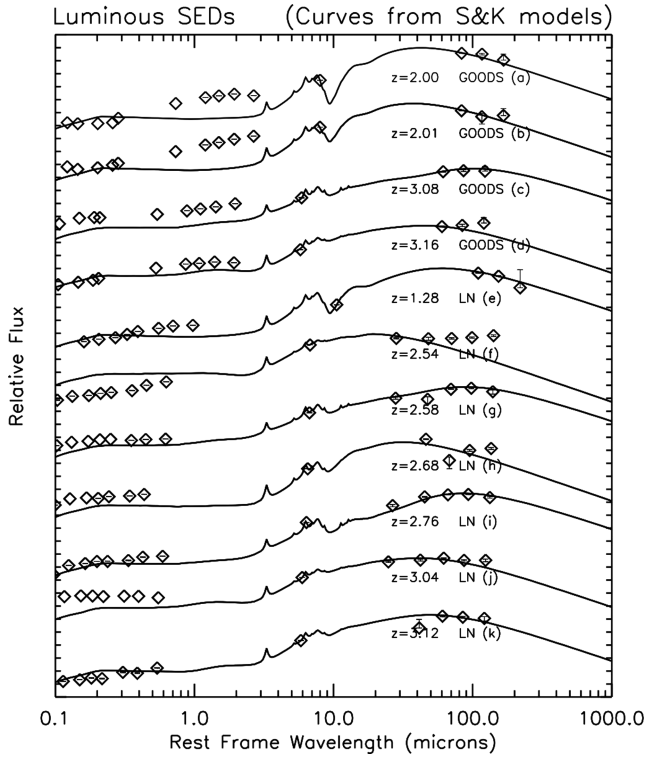

Figure 5. SEDs of the most-luminous sources in the GOODS-N (a)–(d) and LN (e)–(k). As in Figs 2 and 3, we solely plot the upper error bars at 500 μm for sources (a)–(e), whose lower error bars are compatible with zero. We similarly plot an upper error bar at 170 μm for LN (k). Luminosities and positions for these sources are presented in Table 4. Seven of these 11 sources are triply secure; two of these are also included in Figs 2 and 3. A brief description of sources (c), (d), (f) and (i) is provided in Section 6. Although some of the ultraluminous sources exhibit significant AGN activity, we have applied S&K model fits, as discussed in Section 7. As in Figs 2 and 3, we have weighted the 24-μm data only one-quarter as heavily as the longer wavelengths. Observational data shortwards of 24 μm are plotted for reference but not used in fitting.

2–8 keV flux of 22.4×10^{-18} W m^{-2} for the source, jointly about 20 times lower than the visible flux. Owen & Morrison (2008) detected a 20-cm continuum radio flux density of 64 μJy from this source, within an apparent size of <1.5 arcsec FWHM, ruling out obvious ambient emission that might have indicated lensing. The XID catalogues of Roseboom et al. (2010) show a relatively weak neighbouring SPIRE source at a distance of 26 arcsec and a source comparable in IR brightness to LN 4241 but at a separation of ∼34 arcsec. Because of their relatively large displacement, these and other ambient galaxies are unlikely to contribute appreciably to the SPIRE flux densities assigned to LN (j) by Roseboom et al. (2010). All this gives confidence that both the visible and the IR flux comes from the same source, that there is no lens magnification and that we are indeed dealing with an unlensed ultraluminous source with IR luminosity $\sim 1.8 \times 10^{13}\,L_\odot$. The simplest explanation for these data is that we are viewing a QSO with a surrounding torus along a sightline coinciding with the torus axis. The visible light reaches us directly along this axis; the IR emission comes from dust heated in part by the QSO and possibly also by massive star formation.

The GOODS-N source (c), with equatorial coordinates (J2000.0) 188.990097/62.17342, is cited by Barger et al. (2008) as having spectroscopic redshift $z = 3.075$. The 24-μm flux density listed in the Barger catalogue is 109 μJy. The rest-frame 2–8 keV luminosity assigned to this source by Trouille et al. (2008) is 3.464×10^{36} W $\sim 9.01 \times 10^9\,L_\odot$, but their paper provides no rest-frame 0.5–2 keV luminosity. The nearest SPIRE source listed in the XID catalogues lies at a distance of 35 arcsec, where its contribution to our primary galaxy's flux listed in the XID catalogue can at the most be minor. Our primary source also displays weak X-ray fluxes, but Morrison et al. (2010) list no 20-cm source within 3.5 arcmin. Integrating the flux densities indicated by the fitted SED in Fig. 5 leads to an IR luminosity of $6.0 \times 10^{12}\,L_\odot$.

One of our ultraluminous sources [LN (f)] has previously been discussed by Polletta et al. (2006). They observed the Lockman SWIRE source at (J2000.0) 161.041521/58.87355 with *Chandra* and detected a flux of $(2.7 \pm 1.1) \times 10^{-15}$ erg cm^{-2} s^{-1} in the 0.3–8 keV range. The *Spitzer* 24-μm flux is 4.0 mJy, strong for a source at spectroscopic redshift 2.54 and much brighter than anything within 1 arcmin of its location. Because of its initial detection by *Spitzer*, the authors characterize the source as an IR-selected Compton-thick active galactic nucleus (AGN) on the basis of the rest-frame hydrogen column density, which they estimate to be $N_{\rm H} \sim 3 \times 10^{24}$ cm^{-2} with an uncertainty envelope extending a factor of 3× lower and arbitrarily higher. The IR luminosity derived on the basis of our SPIRE and PACS observations (see Fig. 5 and Table 4) is $2.0 \times 10^{13}\,L_\odot$. It appears to be fairly well isolated in the IR, the nearest comparably bright 250-μm source being located 0.5 arcmin away .

Some of these ultraluminous galaxies could be lensed but a first look has not yet revealed these in our sample. The GOODS-N source (d), with coordinates (J2000.0) 189.309509/62.20232, is cited by Barger et al. (2008) as having a spectroscopic redshift $z = 3.157$. Again, ambient nearby sources have relatively weak SPIRE fluxes unlikely to appreciably affect the SPIRE flux attributed to our source of primary interest. Another source only ∼10 arcsec away is also noted in the NASA/IPAC Extragalactic Data base. This appears not to have a measured 24-μm flux and is not listed by Barger et al. (2008). However, Law et al. (2007) have included this source in their discussion of distant irregular galaxies. The object designated as BX 150 appears elongated roughly along a north/south direction, is ∼0.5 arcsec long with an aspect ratio roughly 2:1 and has a redshift $z = 2.28$. At optical wavelengths, it is 1.3 mag fainter than the ultraluminous IR source and, at its rather high displacement of ∼10 arcsec, it is unlikely to provide significant lensing. With this proviso, the intrinsic IR luminosity of GOODS-N (d) appears to be $\sim 1.1 \times 10^{13}\,L_\odot$.

Fig. 5 provides the SEDs of these ultraluminous sources. Our combined surveys of GOODS-N and LN cover ∼0.47 deg^2, or one part in 85 000 of the sky. Given that we observe several high-luminosity sources in the small area covered, it suggests that approximately 10^6 sources in the IR luminosity range $\sim 10^{13}\,L_\odot$ should be observable in the Universe, at redshifts $z = 2.5$–3 at the current epoch. The number of comparably luminous sources observable at lower redshifts appears to sharply decline.

It is unlikely that three selection effects inherent in our observations cast this conclusion into serious doubt:

(i) The first is that Fig. 4, on which the conclusion is based, only includes sources detected at all three SPIRE wavelengths. For highly redshifted sources, the 100-μm IR emission peak is redshifted into the 500-μm range, favouring the detection of galaxies at all three wavelengths, including 500 μm.

(ii) However, compensating for this effect, lower redshift sources are more readily detected by a factor inversely proportional to

Table 4. Data on luminous galaxies whose SEDs appear in Fig. 5, listed as in previous tables. The GOODS sources have spectroscopic redshifts, as do LN (f) and (j). The rest of the LN sources have photometric redshifts. The sources GOODS (a) and LN (i) correspond to the sources GOODS (L) and LN (I) shown in the previous figures and tables.

ID	RA	Dec.	z	$L_{\rm bolometric}$ ($L_\odot$)	SFR ($M_\odot$ yr^{-1})	$M_{\rm dust}$ ($M_\odot$)	Π_{250}	Π_{350}	Π_{500}	Radius (kpc)	A_v	$\mathrm{Log}_{10}(n_{hs} \times \mathrm{cm}^3)$
GOODS (a)	189.0764	62.2640	2.0000	2.0×10^{13}	3400	6.0×10^7	0.82	0.71	0.33	1.0	119.0	2.0
GOODS (b)	189.1483	62.2400	2.0050	2.5×10^{13}	4200	3.6×10^7	0.69	0.24	0.38	1.0	71.0	2.0
GOODS (c)	188.9901	62.1734	3.0750	6.3×10^{12}	1000	2.0×10^9	1.61	1.22	0.84	15.0	18.0	4.0
GOODS (d)	189.3096	62.2024	3.1569	1.3×10^{13}	2000	4.0×10^7	0.57	0.55	0.84	3.0	9.0	2.0
LN (e)	161.7059	59.3247	1.28	1.3×10^{13}	2100	3.2×10^8	0.99	0.85	0.20	3.0	72.0	2.0
LN (f)	161.0415	58.8735	2.28	2.5×10^{13}	3400	4.1×10^5	0.98	1.10	1.71	0.3	6.7	2.0
LN (g)	161.5408	58.7950	2.58	1.3×10^{13}	2000	2.0×10^9	0.82	0.95	0.58	15.0	18.0	4.0
LN (h)	160.9635	58.9555	2.68	2.5×10^{13}	4300	8.8×10^6	0.18	0.95	0.96	0.3	144.0	2.0
LN (i)	161.8667	58.8704	2.76	2.5×10^{13}	4300	4.9×10^9	0.91	0.96	0.77	9.0	120.0	4.0
LN (j)	161.5541	58.7886	2.96	2.0×10^{13}	3100	4.0×10^7	0.76	0.61	0.60	3.0	9.0	3.0
LN (k)	161.8259	59.2771	3.12	1.3×10^{13}	2000	8.0×10^7	0.98	0.70	0.54	3.0	17.8	2.0

luminosity distance squared. Although these two effects partially cancel, high-luminosity sources should be more readily detected at low than at high redshifts.

(iii) The XID catalogues search for SPIRE sources solely at locations where *Spitzer* 24-μm sources exhibit flux densities ≥20 μJy in the GOODS-N field and ≥50 μJy in the LN. We may thus be missing sources at redshifts at which poorly emitting spectral regions are redshifted to 24 μm. At redshifts $z \sim 1.4$, for example, the 9.7-μm silicate absorption dip shown by Spoon et al. (2007) to be prevalent in many ultraluminous infrared galaxies is shifted to 24 μm. This may account for the striking absence of low-luminosity sources, at $z \sim 1.4$, that is, the lack of sources hugging the luminosity distance curve at this redshift in Fig. 4.

7 DISCUSSION

FIR surveys with *Herschel* need to take source confusion and source blending into account, particularly at the longest wavelengths, 350 and 500 μm. The GOODS-N and LN are the two deepest surveys undertaken as part of the HerMES project to date. In these deep fields, crowding of sources presents especially serious problems. In establishing a set of criteria that assess source blending, we have taken a preliminary step towards estimating the utility of the survey data for different purposes. This has proven itself useful in our analysis of the ultraluminous galaxies, some of which we described in Section 6 and whose characteristics are exhibited in Fig. 5 and Table 4. In view of the high IR luminosities we find, it is particularly satisfying that seven of the 11 sources cited turn out to be triply secure, that is, with high purities in all three SPIRE wavebands, and that five of the sources are also observed by the PACS, where blending is not severe, particularly in the 100-μm waveband. In this context, we have placed no upper limit on acceptable values of Π, which are especially high for GOODS-N (c) and LN (f), suggesting especially low ambient source contributions at their locations.

In compiling the SEDs for the GOODS-N and LN, we have elected to work with the S&K models, because they are based on a limited set of well-defined physical parameters. The models thus make predictions that our SEDs may be able to verify, refute or extend. S&K do not specifically address the effects of adding an AGN component to a starburst model. However, they do provide a starburst fit for NGC 6240 and propose that addition of a small AGN component could provide an improved fit. Most starbursts generally also exhibit some AGN activity. Perhaps because of this, the S&K models appear to provide reasonable fits. The major weakness of the S&K models, as well as that of all others, tends to be the difficulty in accounting for the seemingly random relationship between the IR and optical portions of the SEDs that is so apparent in Figs 2, 3 and 5.

We investigated the relationship between flux-density ratios at optical and FIR wavelengths in high- and low-luminosity galaxies. Present theory suggests that starbursts involve stellar mass distributions obeying the Salpeter initial mass function (Zinnecker & Yorke 2007). The drop in luminosities from the most massive O-type stars with mass ∼120 $M_\odot$ to the early B-type stars at 10 $M_\odot$ can then be shown to be roughly in a ratio of 500:1, that is, with a contrast considerably higher than that of the mass ratio, roughly 12:1. The highest mass ranges will thus be depleted most rapidly, ending their lives in supernova explosions in which at least some of the dust will be destroyed or expelled from the galaxy. The most-luminous galaxies found using our SEDs and their associated redshifts would thus be expected to be the very youngest as well as those most densely shrouded by dust, that is, having the lowest fractional optical luminosities. To test this hypothesis, we restricted ourselves to galaxies with total bolometric luminosities $L > 10^{12}\,L_\odot$, as these have long been considered likely starburst mergers, albeit with potential contributions from AGNs (Sanders & Mirabel 1996). In Table 5, we compare the flux density ratios for the most- and least-luminous sources in three redshift bins. It is evident that larger ratios correspond to more luminous sources at all redshifts, but that these differences greatly diminish at lower redshifts. This finding is both new and significant. It indicates evolutionary trends that may need to be incorporated into more advanced models of starbursts designed to yield SEDs, which not only mirror observed ratios of optical

Table 5. Ratios ($R \equiv F_{\rm FIR}/F_{\rm optical}$) of SPIRE flux densities (consistently measured at 250 μm to minimize source blending) to optical flux densities at a rest wavelength ∼3000 Å measured, respectively, at 4500, 6100 and 7600 Å for successively larger redshifts. These three wavelengths were chosen to represent the visible spectra and avoid the Balmer jump at 3650 Å. For each redshift bin, we compare the flux density ratio for the $N/2$ most-luminous galaxies ($R_{\rm Bright}$) to that of the $N/2$ least-luminous galaxies ($R_{\rm Dim}$), where N is the total number of $L > 10^{12}\,L_\odot$ sources.

z	N	$R_{\rm Bright}$	$R_{\rm Dim}$	$R_{\rm Bright}/R_{\rm Dim}$
$0.95 < z < 1.05$	18	64 500	72 000	0.90
$1.9 < z < 2.1$	18	62 500	17 600	3.6
$2.4 < z < 2.8$	10	62 300	5920	11

to IR emission, but also define a galaxy's place in its evolutionary history.

Fig. 4 provides a capsule history of galaxy evolution over cosmological epochs for the sample included in our two deep surveys. The shapes of these distributions are nearly identical in the LN and GOODS-N, which motivated us to plot both in the same figure. A glance confirms that sources having the highest luminosities are found at highest redshifts, that is, earliest epochs. Luminosities higher than $10^{13}\,L_{\odot}$ are generally observed at redshifts $z \sim 2$–3.2, the highest redshifts reached in our surveys.

8 CONCLUSIONS

Confusion, which can be troubling at 250 μm, becomes increasingly severe at 350 and 500 μm. Yet the data at these longer wavelengths are particularly important, given how little is known about this spectral domain. We believe that the triply-secure sources listed in Tables 2–4 will be in demand for follow-on studies that X-ray astronomers, spectroscopists and others may wish to undertake on sources known to be especially free of confusion.

With SPIRE photometry data in hand along with XIDs at several shorter wavelengths, we have constructed SEDs for a handful of trustworthy sources in the GOODS-N and LN regions. Many of these can be fitted by starburst SED models, such as those created by S&K, which yield information on luminosity, dust mass and size. Figs 4 and 5 show a number of ultraluminous galaxies with $L_{\rm IR} \sim 10^{13}\,L_{\odot}$. Although these are extreme systems, they do not appear to deviate from the general distribution at high redshift. A major strength of the deep HerMES projects is their ability to obtain reliable source luminosities and SFRs based on flux densities in the IR and at auxiliary wavelengths as well as redshifts compiled in the XID catalogues.

ACKNOWLEDGMENTS

This work is based in part on observations made with *Herschel*, a European Space Agency Cornerstone Mission with significant participation by the NASA. Support for this work was provided by the NASA through an award issued by JPL/Caltech.

The SPIRE has been developed by a consortium of institutes led by Cardiff University (UK) and including Univ. Lethbridge (Canada); NAOC (China); CEA, OAMP (France); IFSI, Univ. Padua (Italy); IAC (Spain); Stockholm Observatory (Sweden); Imperial College London, RAL, UCL-MSSL, UKATC, Univ. Sussex (UK); and Caltech/JPL, IPAC, Univ. Colorado (USA). This development has been supported by national funding agencies: CSA (Canada); NAOC (China); CEA, CNES, CNRS (France); ASI (Italy); MCINN (Spain); SNSB (Sweden); STFC (UK); and NASA (USA).

We thank the referee of this paper, Stephen J. Messenger, for his incisive comments and helpful recommendations.

REFERENCES

Barger A. J., Cowie L. L., Wang W.-H., 2008, ApJ, 689, 687
Béthermin M., Dole H., Cousin M., Bavouzet N., 2010, A&A, 516, 43
Buat V. et al., 2010, MNRAS
Fixsen D. J. et al., 1998, ApJ, 508, 123
Griffin M. et al., 2010, A&A, 516, 43
Kennicutt R., 1998, ARA&A, 36, 189
Law D. R., Steidel C. C., Erb D. K., Pettini M., Reddy N. A., Shapley A. E., Adelberger K. L., Simenc D. J., 2007, ApJ, 656, 1
Marsden G. et al., 2009, ApJ, 707, 1729
Morrison G. E., Owen F. N., Dickinson M., Ivison R. J., Ibar E., 2010, ApJS, 188, 178
Oliver et al., 2010, A&A, 518, L2
Owen F. N., Morrison G. E., 2008, AJ, 136, 1889
Pilbratt G. L. et al., 2010, A&A, 518, L1
Poglitsch A. et al., 2010, A&A, 518, L2
Polletta M. et al., 2006, ESASP, 604, 807
Roseboom I. et al., 2010, MNRAS, submitted
Sanders D. B., Mirabel I. F., 1996, ARA&A, 34, 749
Siebenmorgen R., Krügel E., 2007, A&A, 461, 445 (S&K)
Spoon H. W. W., Marshall J. A., Houck J. R., Elitzur M., Hao L., Armus L., Brandl B. R., Charmandaris V., 2007, ApJ, 654, L49
Strazzullo V., Pannella M., Owen F. N., Bender R., Morrison G. E., Wang W.-H., Shupe D. L., 2010, ApJ, 714, 1305
Takeuchi T. T., Ishii T. T., 2004, ApJ, 604, 40
Trouille L., Barger A. J., Cowie L. L., Yang Y., Mushotzky R. F., 2008, ApJS, 179, 1
Zinnecker H., Yorke H., 2007, ARA&A, 45, 481

This paper has been typeset from a TEX/LATEX file prepared by the author.